Primary, Scatter, and Penetration Characterizations of Parallel-hole and Pinhole Collimators for I-123 SPECT

Arda Könik[a], **Benjamin Auer**[b], **Jan De Beenhouwer**[c], **Kesava Kalluri**[b], **Navid Zeraatkar**[b], **Lars R Furenlid**[d], **Michael A. King**[b]

[a]Dana Farber Cancer Institute, Department of Imaging, Boston, MA, USA, 02215

[b]University of Massachusetts Medical School, Department of Radiology, Worcester, MA, USA, 01655

[c]University of Antwerp, imec-Vision Lab, Antwerp, Belgium

[d]University of Arizona, College of Optical Sciences, Tucson, AZ, USA, 85719

Abstract

Multi-pinhole (MPH) collimators are known to provide better trade-off between sensitivity and resolution for preclinical, as well as for smaller regions in clinical SPECT imaging compared to conventional collimators. In addition to this geometric advantage, MPH plates typically offer better stopping power for penetration than the conventional collimators, which is especially relevant for I-123 imaging. The I-123 emits a series of high-energy (>300 keV, ~2.5% abundance) gamma photons in addition to the primary emission (159 keV, 83% abundance). Despite their low abundance, high-energy photons penetrate through a low-energy parallel-hole (LEHR) collimator much more readily than the 159 keV photons, resulting in large downscatter in the photopeak window. In this work, we investigate the primary, scatter, and penetration characteristics of a single pinhole collimator that is commonly used for I-123 thyroid imaging and our two MPH collimators designed for I-123 DaTscan imaging for Parkinson's Disease, in comparison to three different parallel-hole collimators through a series of experiments and Monte Carlo simulations. The simulations of a point source and a digital human phantom with DaTscan activity distribution showed that our MPH collimators provide superior count performance in terms of high primary counts, low penetration, and low scatter counts compared to the parallel-hole and single pinhole collimators. For example, total scatter, multiple scatter, and collimator penetration events for the LEHR were 2.5, 7.6 and 14 times more than that of MPH within the 15% photopeak window. The total scatter fraction for LEHR was 56% where the largest contribution came from the high-energy scatter from the back compartments (31%). For the same energy window, the total scatter for MPH was 21% with only 1% scatter from the back compartments. We therefore anticipate that using MPH collimators, higher quality reconstructions can be obtained in a substantially shorter acquisition time for I-123 DaTscan and thyroid imaging.

1. Introduction

While clinical SPECT imaging is commonly performed on general-purpose systems using parallel-hole or cone/fan-beam collimators, most small-animal SPECT systems employ multi-pinhole (MPH) collimators (Franc et al., 2008) because of the improved sensitivity-

resolution trade-off offered for a smaller volume of interest (VOI) (Van Audenhaege et al., 2015). With the same motivation, clinical SPECT systems using MPH collimators have been designed to target smaller regions in the body such as the heart (Erlandsson et al., 2009; Bhusal et al., 2019; Bocher et al., 2010; Bowen et al., 2013; Ogawa and Ichimura, 2014), the breast (van Roosmalen et al., 2017; Tornai et al., 2003; van Roosmalen et al., 2016) and the brain (Chen et al., 2017; Chen et al., 2018; King et al., 2016; Stam et al., 2018). Unlike the general-purpose systems, these dedicated SPECT systems use the detector space more efficiently, hence can provide better sensitivity-resolution trade-off within a smaller VOI.

In addition to this geometric advantage, MPH collimator plates typically offer better stopping power for penetration than the conventional (i.e., parallel-hole and cone/fan-beam) collimators, which have thousands of holes separated by thin lead alloy walls (septa) resulting in the majority of the collimator being composed of air and hence allowing a large amount of collimator penetration. In comparison, except for the pinholes, MPH plates are entirely made of lead or tungsten alloy. While this difference in collimation may not be relevant for most clinical SPECT applications using Tc-99m with 140 keV low-energy primary emissions, where conventional collimators already provide sufficient collimation (Pandey et al., 2015), efficient collimation becomes very important when higher energy emissions are involved, as in the case of I-123. In addition, most MPH collimator plates are made of tungsten (μ_{500}: 2.66 cm^{-1}, ρ: 19.3 g/cm^2), which is about 1.5 times more attenuating than the same thickness of lead (μ_{500}: 1.82 cm^{-1}, ρ: 11.3 g/cm^2) used in conventional collimators at energies >500 keV (computations are performed based on pure tungsten and lead using XCOM, https://physics.nist.gov/PhysRefData/Xcom).

I-123 is an important radionuclide commonly used in clinical SPECT applications such as thyroid, brain perfusion, and dopamine transporter (DAT) imaging, which emits a series of high-energy (>300 keV, ~2.5% abundance) gamma photons in addition to the primary photons (159 keV, 83% abundance) (Gregory et al., 2017). Despite the low abundance of the high-energy photons, they penetrate through the low-energy parallel-hole collimator approximately 15 times more than the primary photons since the attenuation of the high-energy photons in the collimator is much less than the primary photons (Van Holen et al., 2009). Many of these high-energy photons pass through the crystal, undergo Compton scattering from the layers behind the crystal (e.g., photo-multiplier tubes – PMTs and associated electronics), and are then detected by re-entering the crystal with a lower energy within the photopeak window contaminating the projection data. Among these high-energy emissions, the most abundant one is at 529 keV (1.4% abundance) with a backscatter peak at 172 keV (180° Compton scatter) falling into the 20% photopeak window (143–175 keV) of the primary photons. These events are defined as backscatter, a special case of downscatter (detection of the high energy photons after scattering). Depending on the collimator employed and the crystal thickness, the magnitude of backscatter can be very high. Using Monte Carlo simulations a backscatter fraction of approximately 30% (Cot et al., 2004) and a total scatter counts larger than the primary counts (Tanaka et al., 2007) were reported for the low-energy high-resolution (LEHR) collimator.

The backscatter from I-123 high-energy photons is a well-known and studied problem. Some research suggests the usage of medium-energy collimators to reduce the downscatter

(including backscatter) despite their inferior sensitivity and resolution characteristics (Snay et al., 2011; Gregory et al., 2017) or implementing downscatter correction if low-energy collimators are used (Dobbeleir et al., 1999; Small et al., 2006). For the I-123 DAT imaging, the Society of Nuclear Medicine and Molecular Imaging, SNMMI (Djang et al., 2012) and the European Association of Nuclear Medicine, EANM (Darcourt et al., 2010) guidelines recommend the usage of low-energy collimators and fan-beam, if available. Both guidelines also recommend dedicated systems for the I-123 DAT imaging.

The research on the scatter characteristics of the I-123 high-energy photons appears to be limited to conventional collimators without considering the pinhole collimators. In this work, we are aiming to fill this gap by investigating the primary, scatter, and penetration characteristics of a single pinhole collimator that is commonly used for I-123 thyroid imaging and our MPH collimators designed for I-123 DAT imaging (King et al., 2016; Könik et al., 2018), in comparison to parallel-hole collimators through a series of experiments and Monte Carlo simulations. As detailed in the following section, we obtained the projection images and energy spectra of an I-123 capsule for different collimators of a SPECT system through experimental measurements and simulations. Once we verified our simulation model based on the close agreement of these datasets, we performed the simulations of an I-123 point source and I-123 DAT (or DaTscan™, GE) distribution for quantification of primary, scatter, and penetration events for the parallel and pinhole collimators.

2. Methods

2.1 Experimental Acquisitions of an I-123 source

We acquired projections of the background (without a source) and an I-123 capsule source of ~0.2 mCi on a dual-head SPECT/CT system (Philips, BrightView) using three different parallel-hole collimators and a pinhole collimator: LEHR, medium-energy general-purpose (MEGP), high-energy general-purpose (HEGP), and single pinhole (SPH). Table 1 summarizes the specifications of these collimators. The capsule source was placed on the patient table ~10 cm away from the parallel-hole collimator faces and the aperture of the pinhole collimator. The projections of this source were simultaneously acquired using the LEHR/SPH and MEGP/HEGP collimator pairs at 180° mode over 20 minutes. The same acquisition protocol was followed for the background measurements. The energy spectra and projections presented in this work are obtained after the subtraction of the background counts from the corresponding source projections followed by their decay correction. In this way, a total of 7.4, 1.6, 1.0 and 0.78 million counts were collected within the full spectrum for LEHR, MEGP, HEGP, and SPH respectively. The corresponding values within the 15% photopeak energy window (147–171 keV) were 0.95, 0.59, 0.52, and 0.48 million counts, respectively.

2.2 Modeling of the SPECT head and collimators

We modeled the geometry of the Brightview SPECT system with the collimators mentioned in the previous section using the Geant4 Application for Tomographic Emission (GATE) Monte Carlo simulation toolkit (Jan et al., 2004) based on manufacturers' specifications and

our physical measurements. We also modeled two of our MPH collimator designs with 9 and 16 pinhole apertures in a 2-cm thick tungsten alloy (tungsten 90% + copper 10%, density: 18.2 g/cm^3) plate, herein referred to as 9MPH and 16MPH collimators, respectively, aimed for DAT imaging (Könik et al., 2018; Könik et al., 2017).

The walls of the LEHR collimator are constructed by folding lead alloy (lead 95% + antimony 5%, density: 11.1 g/cm^3) foils, which forms double septa on two opposing sides and single septa on the other four sides of the hexagon holes resulting in uneven stopping power. The MEGP and HEGP collimators are built by casting lead, where all six walls are formed by single septa providing a uniform stopping power – except at the vertices of the hexagon. We implemented these construction details in our simulation models as shown in Figure 1. The inserts in this figure show the measured projections of the capsule source for the full energy spectrum and 15% photopeak window. The "star" artifacts in the projections (the image scale was adjusted to make the effect more visible) follow the exact same directions as denoted with the blue arrows. These directions indicate the shortest attenuation path in the collimators: four single-foil septa of the LEHR and perpendicular photon incidence on six septa of the MEGP/HEGP. Another detail to note is that the LEHR hexagon holes are oriented in 90° with respect to the holes of the MEGP and HEGP collimators. Assuming an equal surface area for the collimator plane and the NaI(T1) crystal (540 × 400 mm^2), 354 × 350, 146 × 93 and 112 × 72 holes were placed in the LEHR, MEGP and HEGP collimators, occupying 74%, 64%, and 47% (as shown in Table 1) of the collimator volumes, respectively.

The geometry of the SPH collimator was first generated in Solidworks^R software (https://www.solidworks.com/) based on the Computer-Aided Design (CAD) drawing provided by the manufacturer and then was converted into the STL format (triangular surface meshes) and imported into GATE. We used the same method for modeling the geometry of 9MPH and 16MPH collimators in GATE. Figure 2 presents the geometry of these collimators modeled and visualized in GATE. The specifications of the collimator insert for the SPH and the collimator plate for MPH are listed in Table 1. The volumetric proportion of air for the MPH was calculated within the dashed box indicated over the collimator plates in Figure 2. The SPH collimator insert is considerably smaller than this region, hence the larger air volume (10%) compared to MPH (2.2% and 2.5%). In addition to these properties, knife-edge pinholes were modeled for both SPH and MPH collimators.

For modeling the compartments behind the 0.925-cm thick crystal (i.e., back compartment), we followed the "intermediate model" described in (Rault et al., 2011), which represents the compartments as multiple layers and PMTs by a box filled with a mixture of materials. Their study shows that the intermediate model provided the best quantitative (sensitivity and spatial resolution) agreement with the measurements for the I-123 source. Herein, the back compartments consist of a light guide (0.925 cm), PMTs, and electronics, which are enclosed in the lead and aluminum casings as indicated in Figure 2.

2.3   Monte Carlo simulations

GATE simulations presented in this work modeled all the relevant physics including attenuation (photo-electric absorption, Compton and Rayleigh scattering), collimator

penetration, and fluorescent x-ray secondary emission (e.g., characteristic x-rays emitted by the collimators and shielding). In addition, the intrinsic energy and spatial resolutions of the detector were modeled by sampling from Gaussian distributions of 10% FWHM at 159 keV and 3 mm FWHM, respectively. The energy resolution assumed to follow a linear relation with the gamma energy. When a gamma photon undergoes multiple interactions (hits) in the crystal the energy for this event is summed and the event position is obtained from the energy-weighted centroid of the different interactions. We used the 14 most abundant gamma emissions to model the I-123 emission spectrum accurately (Be et al., 2004).

2.3.1 Capsule source simulations—To validate our simulation setup, we modeled the I-123 capsule source by a cylindrical source (diameter: 0.68 mm and height: 0.68 mm in sucrose with a density of 1.6 g/cm^3) with uniform activity and placed it at 10 cm distance from collimator face and pinhole aperture, replicating the experimental acquisitions above. For this purpose, we compared the energy spectra (0 – 700 keV) and projections (energy window: 159 keV$\pm$7.5%) obtained from the measurements and simulations. In addition to the SPECT heads, we modeled the attenuation of the capsule and its 2 mm thick plastic container (measured density: 1.5 g/cm^3), and 9.5 mm thick carbon-fiber patient table (simulated density: 0.55 g/cm^3) as these introduce attenuation (i.e., absorption and scatter) and alter the energy spectra at energies mainly below the photopeak region.

2.3.2 Point-source simulations—In addition to the capsule source simulations, we simulated the projections of a point source in air to determine the scatter and penetration characteristics in the absence of attenuation media other than the components of the SPECT head. Hence, we did not include the attenuating objects mentioned for the capsule source simulations. In this set of simulations, we also included the 9MPH and 16MPH collimators. We placed the point source at 14 cm from the parallel-hole collimator faces and the aperture plane of the pinhole collimators, which is also the focal point for the MPH collimators. As explained in the following sections we used the data from the point source simulations to obtain the scatter, primary and collimator penetration counts for a range of photopeak energy windows and for the full energy spectrum.

2.3.3 DaTscan simulations—We obtained the projections of the XCAT digital phantom (Segars et al., 2010) approximately modeling a normal DaTscan distribution with the activity concentration ratios of *striatum : salivary glands : lungs : liver : background = 8 : 4 : 2 : 6 : 1* (Sydoff et al, 2013). We represented this activity distribution with a voxelized phantom covering the head and torso, as shown in Figure 3. In order to avoid volume overlaps between the attenuation phantom and the rotating SPECT head, instead of using a voxelized attenuation phantom, we used a mesh modeling (STL) of the XCAT attenuation phantom derived from its native NURBS data (Auer et al., 2018). Figure 3 at the right shows the STL-based anatomy with the organs listed above. This anatomy was then converted to attenuation map by segmenting it into five different attenuation coefficient regions: water, brain, lung, bone and air. The compositions of these regions were predefined in GATE.

For each collimator, 20 equally spaced projections were obtained over 360° around the head at a radius of rotation of 14 cm. The projection images from the parallel-hole collimators included the entire brain and a small portion of the salivary glands as seen

in clinical images. While the images from the SPH collimator also included the entire brain, the MPH collimators imaged mainly the inner region of the brain focusing on the center of the striatum. That is, the common field-of-view (FOV) of all the MPH pinholes was the inner brain although some of the pinholes imaged regions beyond this common FOV depending on the projection view in the acquisition. In addition, 16MPH had 30% background/background and 28% background/striatum multiplexing in the projection data, while 9MPH was nearly multiplex-free with 3% background/background multiplexing only and no background/striatum multiplexing.

2.3.4   Analyses—We developed a stand-alone analysis based on ROOT (http://root.cern.ch) to determine the primary and scatter counts from the object (phantom), collimator, shielding, and back compartments for a range of energy windows over the 159 keV photopeak (10, 15, 20 and 25%) and for the full energy spectmm (0–700 keV). We also included collimator penetration for the point source in air and the XCAT DaTscan simulations in this analysis. To do this, we used a modified version of the GATE code (De Beenhouwer et al., 2009) to obtain the original emission energies of the scatter, primary, and collimator penetration counts, as this information is not available by default in GATE.

We reported these results in terms of fractions with respect to the total counts: scatter fraction *(100× scatter counts / total counts)* as described in section 3.3, multiple scatter fraction *(100× multiple scatter / total counts)* as described in section 3.4, primary score *(primary$_{159keV}$ / total counts)× (primary$_{159keV}$ sensitivity)* as described in section 3.5, and collimator penetration *(100× collimator penetration counts / total counts)* as described in section 3.6.

3.   Results

3.1   Verification of the simulation setup

We obtained a reasonable agreement between the measurements and simulations of the I-123 capsule source for the energy spectra and projections. Figure 4 shows the energy spectra side by side for the four different collimators of the BrightView SPECT system. Note, the BrightView specifications list the operation energy range as 56–920 keV. Hence, the measured spectra should be ignored below 56 keV. In both sets of spectra the counts are normalized by the maximum count level of the LEHR. Apart from the overall visual agreement between the measured and simulated spectra, the relative spatial distribution of counts around the photopeak energy from different collimators are nearly the same. In the same figure, measured and simulated projections are presented along with their corresponding full-width at half-maximum (FWHM) in horizontal (x) and vertical (y) directions in mm. The difference in FWHMs from measurements and simulations was less than 10%, which is reasonable considering various potential sources of errors such as in modeling the attenuation of the patient bed, capsule dimensions and its distance to collimators, crystal energy resolution as function of energy, Poisson noise in the datasets, and non-Gaussian point spread functions (PSFs) especially for HEGP and MEGP. Note that the HEGP and MEGP projections were smoothed by a Gaussian filter (FWHM: 0.7) prior to FWHM measurements to obtain an approximately Gaussian PSF.

3.2 Energy spectra

Figure 5 shows the energy spectra obtained from the simulations of an I-123 point source at a distance of 14 cm from the parallel collimator faces and aperture planes of the SPH, 9MPH, and 16MPH collimators. With the inclusion of the MPH energy spectra, the spectra from the rest of the collimators scaled down dramatically. For example, a 5.5-fold difference is visible between the photopeak of 16MPH and LEHR despite the large downscatter in LEHR counts. For this reason, we also included the energy spectra of the parallel-hole and pinhole collimators, separately.

Figure 6 shows the energy spectra and sum of 20 projection views over 360° obtained from the simulations of the XCAT phantom with I-123 DaTscan distributions for the parallel-hole and pinhole collimators. We show the summed projections to improve the statistics in the images. For the MPH, the striatum is not identifiable from these images because of the striatum/background overlaps among different projection views and the higher noise level per pinhole. For example, the count levels for the 16MPH and single pinhole are 0.36M/16 = 0.0225M and 0.04M per pinhole, respectively.

3.3 Scatter Fraction from individual components

A "scatter" or "scatter event" in this work is defined as a gamma photon undergoing a single or multiple Compton or Rayleigh scattering interactions with matter prior to detection within the defined energy window. That is, the scattered photons not reaching the crystal or being outside the energy window are not counted as scatter event. In this section, we present individual scatter fractions from the XCAT phantom and from different system components such as the collimator, shielding, and back compartments. As indicated in Figure 2, "collimator" refers to the septa of the hexagons in the parallel-hole collimator, the insert in single pinhole collimator, and the plates in MPH collimators; "shielding" is defined as the lead casings on the SPECT head and also the trapezoid supporting the MPH plate; and the back compartments are defined as the components behind the crystal other than the shielding. The individual scatter fractions are based on the scattering from the last volume of interaction prior to detection regardless of being a multi-scattering or single-scattering event. For example, a photon that scattered first in the collimator and then in back compartments, is counted as a single scatter event from the back compartments. The multi-scatter aspect is separately presented in the next section.

The bar graphs in Figure 7 show the scatter fractions of the individual system components obtained from the I-123 point source simulations for a range of photopeak energy windows (10, 15, 20, and 25%) and for the full spectrum (0–700 keV). For example, LEHR total scatter fraction is 31% at 15% energy window, where majority of the scatter is recorded from the back compartments (20%). For the same energy window, the total scatter fraction for the MPH collimators is less than 2%. Similarly, Figure 8 shows the percent scatter fractions for I-123 DaTscan simulation where XCAT brain and torso phantom scatter is also included. In this case, LEHR total scatter fraction is 56% at 15% photopeak energy window where 31% of the scatter is from the back compartments. For the same energy window, the total scatter for 16MPH is 21% with only 1% scatter from the back compartments.

3.4 Multiple scatter

In Figures 7 and 8, scatter fractions in percent for the phantom and different components of the system are presented based on the scatter counts from the last volume of interaction prior to detection. In reality, however, many gamma photons undergo multiple scatter events, which have potentially larger impact in image degradation since multiple scatter can cause further deviation from the original emission direction. We defined multiple scatter events as follows: if a gamma photon undergoes scattering more than once prior to detection within the energy window, it is considered as one multiple scatter event. For example, each of these are considered as a multiple scatter event: $2 \times$ Compton scatter, $2 \times$ Rayleigh scatter, or 1 Rayleigh $+$ 1 Compton scatter. In Figure 9, we present multiple scatter fractions in percent for the I-123 point source and DaTscan simulations, where *total scatter counts = single scatter + multiple scatter*. Based on these results LEHR shows considerably higher multiple scatter fraction than that of the other collimators indicating more impact in the images.

3.5 Primary counts

The primary counts are the unscattered events that reached the detector and counted within the energy window. In this work, we removed the collimator penetration component from the 159 keV primary counts and hence considered only the ones that go through the collimator holes. Therefore, these scatter and penetration-free photons carry uncorrupted information about the position of the emission source. Since I-123 imaging is ideally based on the counts of the primary photopeak photons, a high *primary/total count ratio* and high *primary sensitivity* (159 keV primary counts / total number of emissions) is desirable. We quantified this aspect as *(primary$_{159keV}$ / total counts)$\times$ (primary$_{159keV}$ sensitivity)* and referred to it as "primary 159 keV score". In Figure 10 we show these scores for the I-123 point source and DaTscan simulations after normalizing by the corresponding maximum values of the 16MPH at 25% and 20% energy windows, respectively. By this metric 16MPH outperforms LEHR, MEGP, HEGP, SPH and 9MPH by about 13, 3.7, 3.8, 11, and 1.6 times, respectively, for the DaTscan projections obtained within the 15% and 20% photopeak energy windows. For the point source projections, the corresponding factors were 17, 6.6, 7.1, 18, and 1.6.

3.6 Collimator Penetration

Collimator penetration in this paper is defined as the gamma photons going through the parallel-hole collimator septa, SPH collimator insert, or MPH collimator plate without any interaction and then being detected within the energy window. These photons may or may not have scattered in places other than the collimator before or after collimator penetration. These non-collimated events thus result in image degradation. Figure 11 shows the collimator penetration in percent of the 159 keV and high-energy (HE) photons, separately, for the I-123 point source in air and XCAT DaTscan simulations. Interestingly, for the LEHR collimator, as the energy window gets wider the collimator penetration fraction of the 159 keV decreases while the penetration fraction of the HE increases. The decreasing trend for the penetration fraction of the 159 keV photons is simply because of the increasing total counts (more scatter in wider windows) while 159 keV penetration counts

remain relatively stable. The increasing trend for the penetration fraction of the HE photons can be explained as following: many HE penetration photons scatter in the crystal and escape from it partly depositing their energy, thus falling into the photopeak window. The rate of these events increases as the energy window gets wider. For the other collimators, penetration fractions of the 159 keV photons is nearly constant as the total counts remain about the same, as can be seen from the energy spectra in Figures 5 and 6.

Figure 12 shows the I-123 point source projections of the collimator penetration counts obtained within the 15% photopeak energy window. The projections at the top and bottom rows are for the HE and 159 keV emissions obtained within the 15% photopeak energy window, respectively. A large amount of collimator penetration is recorded from HE for the LEHR collimator. In contrast, MPH collimators have large amount of penetration for the 159 keV photons. However, the penetration counts per pinhole are considerably smaller than the rest of the collimators: 5.8K/pinhole for 9MPH and 4.8K/pinhole for 16MPH. Another observation is that the HE penetration counts are relatively localized for the pinholes mainly because of the penetration through the knife edge and they would have less impact in images compared to widely spread projections of the parallel collimators.

4. Discussion

We verified our Monte Carlo simulation geometry through a comparison of the energy spectra and projection images from the experimental acquisition and simulation of an I-123 source (capsule source). While we made a considerable effort to obtain a close match, reaching an exact agreement between the measurements and simulations was challenging because of many uncertainties or unknowns about the system as briefly mentioned in the results section. Nevertheless, we obtained sufficient agreement for the purpose of our study.

We showed scatter, primary, and penetration characteristics of three different parallel-hole collimators, a single pinhole collimator and two of our MPH collimator designs for a range of energy windows. MPH collimators, especially 16MPH, showed superior performance over the other collimators in every aspect we presented here. We summarized these results for the I-123 point source in air and XCAT DaTscan simulations in Table 2 for the 15% photopeak energy window. For example, total scatter, multiple scatter, and collimator penetration events, from LEHR were 2.5, 7.6 and 14 times more than that of 16MPH for XCAT DaTscan simulations. The major scatter component for LEHR was from the backscatter of the high-energy photons, as other investigators have shown (Cot et al., 2006). All of these events are misplaced in the projections degrading the reconstructed images. In addition to the large amount of collimator penetration, these events are broadly spread across the crystal for the parallel-hole collimators, as shown in the point source projection images obtained from the high-energy collimator penetration counts (Figure 12). Whereas the corresponding projections for SPH and MPH are relatively localized for both 159 keV and high-energy photons, hence less impact would be expected in the reconstructed images.

The Compton scatter can be reduced to some extent through scatter correction methods such as triple energy window (TEW) (Ichihara et al., 1993), but these methods amplify image noise (Hutton el al., 2011). On the other hand, counts from Rayleigh (coherent) scatter and

collimator penetration cannot be corrected based on these energy discrimination methods as in both processes photon energies remain unchanged. However, in practice the impact of Rayleigh scatter is negligible because of narrow-angle scatter and lower contribution to the counts. In these simulations, 80–90% of the total scatter was from Compton scatter only, 1.5–3% from Rayleigh scatter only, and the remaining was a mixture of Compton and Rayleigh scatter.

While the scattering in the phantom is independent of the collimator choice, the phantom scatter fractions presented in Figure 8 vary depending on the collimator as they are obtained from the last volume of interaction. For example, high-energy photons scattered in the phantom are much more likely to penetrate through the LEHR collimator and backscatter than the other collimators studied here. Since these events are recorded as scatter in the back comportment, which is the last scatter volume in this case, LEHR appears to have considerably less phantom scatter compared to the other collimators.

In addition to the image degrading events mentioned above, we defined a metric for the "good events" obtained from scatter and penetration-free 159 keV primary photons, since these are the most valuable counts in the photopeak window. For DaTscan images both high primary ratio and sensitivity of 159 keV photons are desired. Thus, we defined our metric as: *(primary$_{159keV}$ / total counts) × (primary$_{159keV}$ sensitivity)*. In terms of this metric, 16MPH score was about 12 times greater than that of LEFIR for DaTscan as listed in Table 2. Note, however, 16MPH had 30% background/background and 28% background/striatum multiplexing in the projection data, which elevates the counts at the expense of potential multiplexing artifacts. 9MPH on the other hand was nearly multiplex-free with 3% background/background multiplexing only and no background/striatum multiplexing. Hence, the primary scores presented in Figure 10 for MPH should be interpreted effectively between the 16MPH (multiplexed) and 9MPH (multiplex-free) scores reported herein. Also, we did not use baffle (Kench et al., 2011) in the simulation which would reduce the multiplexing.

Another important point is related to the FOV of different collimators. The parallel-hole collimators had larger FOVs than the MPH collimators, receiving additional background counts from regions that were not covered by the limited FOV of the MPH collimators. However, these extra counts that are mainly from other portions of the brain than the striatal region and the salivary glands, and thus are not useful for DAT imaging. In addition, we found that 11, 1, 0.5, 8, 3, and 2% of the total counts for the LEHR, MEGP, HEGP, SPH, 9MPH, and 16MPH, respectively, are from the torso (below the neck) for the 15% photopeak energy window, which are almost entirely scatter counts. For example, in Table 2 the total counts of 16MPH is 2.4 times more than that of LEHR for the DaTscan. For the same data, the striatum counts of the 16MPH is ~5 times more than the striatum counts of the LEHR. Therefore, we expect that the performance difference between MPH and parallel-hole collimators will be even more dramatic for the counts that originated from the striatum.

Thus far we mainly limited our discussion to comparing the LEHR and MPH collimators, while MEGP and HEGP collimators showed ~3 times better primary score than LEHR and

have similar scatter fractions as MPH. However, their primary score, collimator penetration, total count ratio, as well as, spatial resolution obtained from PSFs (Figure 5), were considerably inferior compared to the values for the MPH collimators. Also, SPH had similar primary score as LEHR and lower scatter/penetration characteristics than LEHR.

The results presented in this work are based on the 5 mm pinhole aperture diameter. The FWHMs of SPH and MPH projections were ~11 mm for a point source placed at 14 cm from the aperture. This distance is the focal point of the MPH collimators and also is the radius of rotation (ROR) for the DaTscan simulations. Similarly, for LEHR, the point source was 14 cm away from the collimator face and we measured its FWHM as ~9 mm. Hence smaller apertures could be used to match the resolution of the LEHR at ROR, which would result in slightly lower sensitivity and hence lower primary score than we presented here. We used knife-edge apertures, which allowed considerable penetration from the 159 keV photons forming ring-shaped projections and impacting the spatial resolution, as shown in Figure 12. These rings can be reduced and hence the spatial resolution can be improved by using keel-edge apertures at the expense of decreased sensitivity (Van Der Have and Beekman, 2006) and/or modeling the PSF (Pino et al., 2015).

5. Conclusion

We showed scatter, primary and collimator penetration characteristics of three different parallel-hole collimators, a single pinhole collimator, and two of our MPH collimator designs. Our quantitative results based on verified simulation geometries show that our MPH collimator designs, especially 16MPH, provides superior performance in terms of high primary counts, low penetration, and low scatter counts compared to the parallel-hole or single pinhole collimators. This advantage is further enhanced when only striatum counts considered, which provides the most relevant information for DaTscan imaging. Our findings are encouraging for the usage of the existing and new MPH SPECT systems for I-123 imaging, especially for thyroid and DaTscan imaging. We expect that using MPH collimators, higher quality reconstructions can be obtained in a substantially shorter acquisition time for I-123 DaTscan and thyroid imaging.

Acknowledgement

References

Auer B, Könik A, Fromme TJ, Kalluri KS, Beenhouwer JD, Furenlid LR and King MA IEEE Nuclear Science Symposium & Medical Imaging Conference, 2018), vol. Series)

Be MM, Chiste V, Dulieu C, Kellett MA, Mougeot X, Arinc A, Chechev VP, Kuzmenko NZ, Kibedi T, Luca A and Nichols AL 2004 Monographie BIPM-5 Table of Radionuclides: Bureau International Des Poids et Mesures)

Bhusal N, Dey J, Xu J, Kalluri K, Konik A, Mukherjee JM and Pretorius PH 2019 Performance analysis of a high-sensitivity multi-pinhole cardiac SPECT system with hemi-ellipsoid detectors Med Phys 46 116–26 [PubMed: 30407634]

Bocher M, Blevis IM, Tsukerman L, Shrem Y, Kovalski G and Volokh L 2010 A fast cardiac gamma camera with dynamic SPECT capabilities: design, system validation and future potential Eur J Nucl Med Mol Imaging 37 1887–902 [PubMed: 20585775]

Bowen JD, Huang Q, Ellin JR, Lee TC, Shrestha U, Gullberg GT and Seo Y 2013 Design and performance evaluation of a 20-aperture multipinhole collimator for myocardial perfusion imaging applications Phys Med Biol 58 7209–26 [PubMed: 24061162]

Chen L, Tsui BMW and Mok GSP 2017 Design and evaluation of two multi-pinhole collimators for brain SPECT Ann Nucl Med 31 636–48 [PubMed: 28755084]

Chen Y, Vastenhouw B, Wu C, Goorden MC and Beekman FJ 2018 Optimized image acquisition for dopamine transporter imaging with ultra-high resolution clinical pinhole SPECT Phys Med Biol 63 225002

Cot A, Jane E, Sempau J, Falcon C, Bullich S, Pavia J, Calvino F and Ros D 2006 Modeling of high-energy contamination in SPECT imaging using Monte Carlo simulation IEEE Transactions on Nuclear Science 53 198–203

Cot A, Sempau J, Pareto D, Bullich S, Pavia J, Calvino F and Ros D 2004 Study of the point spread function (PSF) for 123I SPECT imaging using Monte Carlo simulation Phys Med Biol 49 3125–36 [PubMed: 15357186]

Darcourt J, Booij J, Tatsch K, Varrone A, Vander Borght T, Kapucu OL, Nagren K, Nobili F, Walker Z and Van Laere K 2010 EANM procedure guidelines for brain neurotransmission SPECT using (123)I-labelled dopamine transporter ligands, version 2 Eur J Nucl Med Mol Imaging 37 443–50 [PubMed: 19838702]

De Beenhouwer J, Staelens S, Vandenberghe S, Verhaeghe J, Van Holen R, Rault E and Lemahieu I 2009 Physics process level discrimination of detections for GATE: assessment of contamination in SPECT and spurious activity in PET Med Phys 36 1053–60 [PubMed: 19472610]

Djang DS, Janssen MJ, Bohnen N, Booij J, Henderson TA, Herholz K, Minoshima S, Rowe CC, Sabri O, Seibyl J, Van Berckel BN and Wanner M 2012 SNM practice guideline for dopamine transporter imaging with 123I-ioflupane SPECT 1.0 J Nucl Med 53 154–63 [PubMed: 22159160]

Dobbeleir AA, Hambye AS and Franken PR 1999 Influence of high-energy photons on the spectrum of iodine-123 with low- and medium-energy collimators: consequences for imaging with 123I-labelled compounds in clinical practice Eur J Nucl Med 26 655–8 [PubMed: 10369952]

Erlandsson K, Kacperski K, van Gramberg D and Hutton BF 2009 Performance evaluation of D-SPECT: a novel SPECT system for nuclear cardiology Phys Med Biol 54 2635–49 [PubMed: 19351981]

Franc BL, Acton PD, Mari C and Hasegawa BH 2008 Small-animal SPECT and SPECT/CT: important tools for preclinical investigation J Nucl Med 49 1651–63 [PubMed: 18794275]

Gregory RA, Murray I, Gear J, Aldridge MD, Levine D, Fowkes L, Waddington WA, Chua S and Flux G 2017 Objective comparison of lesion detectability in low and medium-energy collimator iodine-123 mIBG images using a channelized Hotelling observer Phys Med Biol 62 17–30 [PubMed: 27973344]

Hutton BF, Buvat I and Beekman FJ 2011 Review and current status of SPECT scatter correction Phys Med Bio 56 R85–112 [PubMed: 21701055]

Ichihara T, Ogawa K, Motomura N, Kubo A and Hashimoto S 1993 Compton scatter compensation using the triple-energy window method for single- and dual-isotope SPECT J Nucl Med 34 2216–21 [PubMed: 8254414]

Jan S et al. 2004 GATE: a simulation toolkit for PET and SPECT Phys Med Biol 49 4543–61 [PubMed: 15552416]

Kench PL, Lin J, Gregoire MC and Meikle SR 2011 An investigation of inconsistent projections and artefacts in multi-pinhole SPECT with axially aligned pinholes Phys Med Biol 56 7487–503 [PubMed: 22080828]

King MA, Mukherjee JM, Konik A, Zubal IG, Dey J and Licho R 2016 Design of a Multi-Pinhole Collimator for I-123 DaTscan Imaging on Dual-Headed SPECT Systems in Combination with a Fan-Beam Collimator Nuclear Science. IEEE Transactions on 63

Könik A, De Beenhouwer J, Mukherjee JM, Kalluri K, Banerjee S, Zeraatkar N, Fromme T and King MA 2018 Simulations of a Multi-Pinhole SPECT Collimator for Clinical Dopamine Transporter (DAT) Imaging IEEE Transactions on Radiation and Plasma Medical Sciences

Könik A, Fromme TJ, Beenhouwer JD, He Y, Banerjee S, Kalluri K, Furenlid LR and King MA IEEE Nuclear Science Symposium and Medical Imaging Conference, 2017), vol. Series)

Ogawa K and Ichimura Y 2014 Simulation study on a stationary data acquisition SPECT system with multi-pinhole collimators attached to a triple-head gamma camera system Ann Nucl Med 28 716–24 [PubMed: 24916488]

Pandey AK, Sharma SK, Karunanithi S, Kumar P, Bal C and Kumar R 2015 Characterization of parallel-hole collimator using Monte Carlo Simulation Indian J Nucl Med 30 128–34 [PubMed: 25829730]

Pino F, Roe N, Aguiar P, Falcon C, Ros D and Pavia J 2015 Improved image quality in pinhole SPECT by accurate modeling of the point spread function in low magnification systems Med Phys 42 703–14 [PubMed: 25652484]

Rault E, Staelens S, Van Holen R, De Beenhouwer J and Vandenberghe S 2011 Accurate Monte Carlo modelling of the back compartments of SPECT cameras Phys Med Biol 56 87–104 [PubMed: 21119230]

Segars WP, Sturgeon G, Mendonca S, Grimes J and Tsui BM 2010 4D XCAT phantom for multimodality imaging research Med Phys 37 4902–15 [PubMed: 20964209]

Small AD, Prosser J, Motherwell DW, McCurrach GM, Fletcher AM and Martin W 2006 Downscatter correction and choice of collimator in 123I imaging Phys Med Biol 51 N307–11 [PubMed: 16912369]

Snay ER, Treves ST and Fahey FH 2011 Improved quality of pediatric 123I-MIBG images with medium-energy collimators J Nucl Med Technol 39 100–4 [PubMed: 21565952]

Stam MK, Verwer EE, Booij J, Adriaanse SM, de Bruin CM and de Wit TC 2018 Performance evaluation of a novel brain-dedicated SPECT system EJNMMI Phys 5 4 [PubMed: 29492787]

Sydoff M, Lizana H, Mattsson S, Stabin MG and Leide-Svegborn S 2013 Determination of the biodistribution and dosimetry of (1)(2)(3)I-FP-CIT in male patients with suspected Parkinsonism or Lewy body dementia using planar and combined planar and SPECT/CT imaging Appl Radiat Isot 82 300–7 [PubMed: 24135637]

Tanaka M, Uehara S, Kojima A and Matsumoto M 2007 Monte Carlo simulation of energy spectra for (123)I imaging Phys Med Biol 52 4409–25 [PubMed: 17634641]

Tornai MP, Bowsher JE, Jaszczak RJ, Pieper BC, Greer KL, Hardenbergh PH and Coleman RE 2003 Mammotomography with pinhole incomplete circular orbit SPECT J Nucl Med 44 583–93 [PubMed: 12679403]

Van Audenhaege K, Van Holen R, Vandenberghe S, Vanhove C, Metzler SD and Moore SC 2015 Review of SPECT collimator selection, optimization, and fabrication for clinical and preclinical imaging Med Phys 42 4796–813 [PubMed: 26233207]

Van Der Have F and Beekman FJ 2006 Penetration, scatter and sensitivity in channel micro-pinholes for SPECT: a Monte Carlo investigation IEEE transactions on nuclear science 53 2635–45

Van Holen R, Staelens S and Vandenberghe S 2009 SPECT imaging of high energy isotopes and isotopes with high energy contaminants with rotating slat collimators Med Phys 36 4257–67 [PubMed: 19810500]

van Roosmalen J, Beekman FJ and Goorden MC 2017 System geometry optimization for molecular breast tomosynthesis with focusing multi-pinhole collimators Phys Med Biol 63 015018 [PubMed: 28994663]

van Roosmalen J, Goorden MC and Beekman FJ 2016 Molecular breast tomosynthesis with scanning focus multi-pinhole cameras Phys Med Biol 61 5508–28 [PubMed: 27384301]
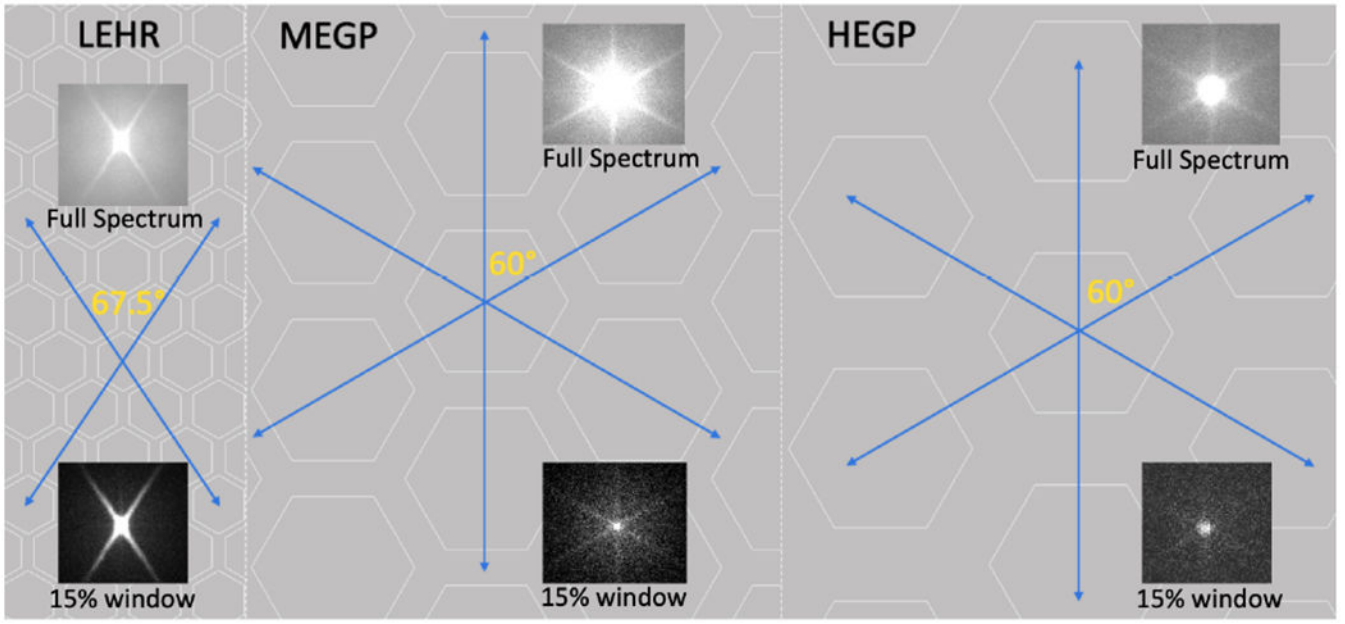
Figure 1.
Foil (LEHR) and cast (MEGP and HEGP) collimators implemented in GATE. Note, LEHR hexagon holes have dual-septa on two sides and are oriented in 90° with respect to the MEGP and HEGP collimators. The blue arrows indicate the directions of the "star artifact" observed in both measured and simulated projections of the capsule source. The inserts here show the measured projections for the 15% energy window and full spectrum (image scale was adjusted for visibility). These blue arrows indicate the directions for the shortest attenuation paths in the collimators: four single-foil septa of the LEHR and perpendicular photon incidence on six septa of the MEGP/HEGP).
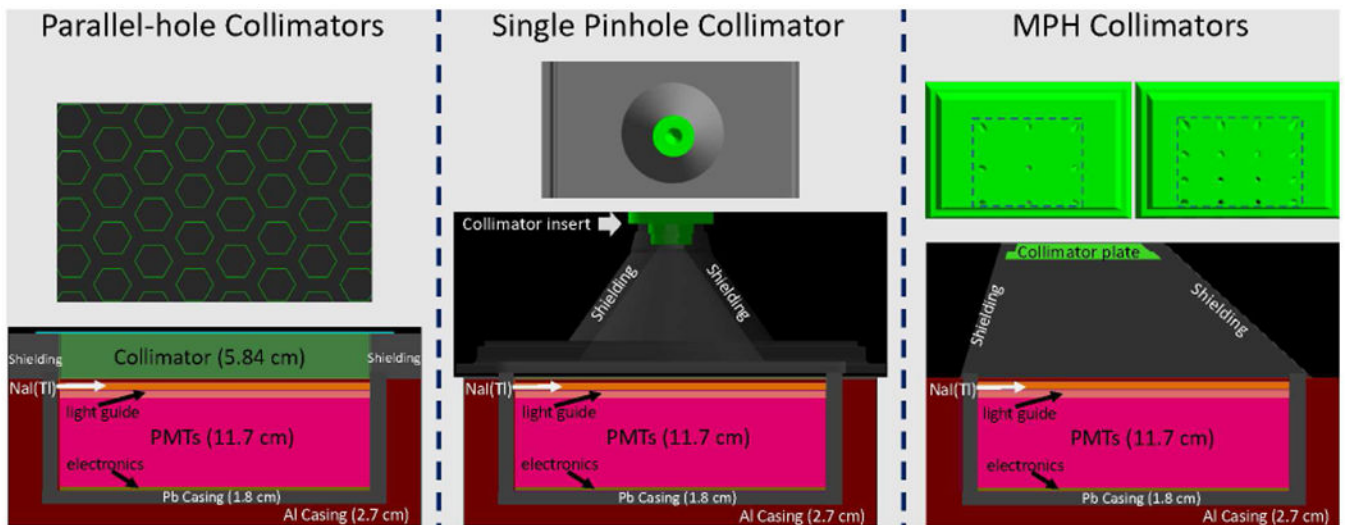
Figure 2.
Screenshots from GATE simulations showing the geometry of the parallel collimators (HEGP is shown), SPH collimator, and MPH collimators with 9 and 16 pinholes. The figures at the bottom show the side view of the collimator and the SPECT camera consisting of the identical NaI(T1) crystal and back compartments (optical coupling – opt., PMTs, and electronics) for all cases. The figures on top show a portion of the top view of the collimators (green).
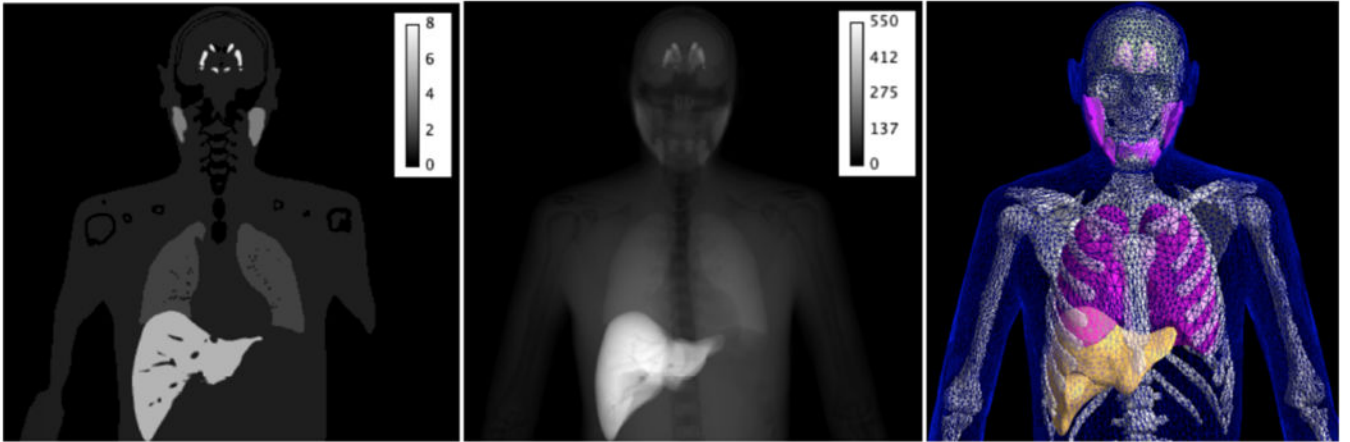
Figure 3.
Center coronal slice (left), summed coronal slices (middle) of the XCAT voxelized activity phantom representing normal DaTscan distribution, and a 3D rendering of the STL representation of the corresponding anatomy (right) showing organs.
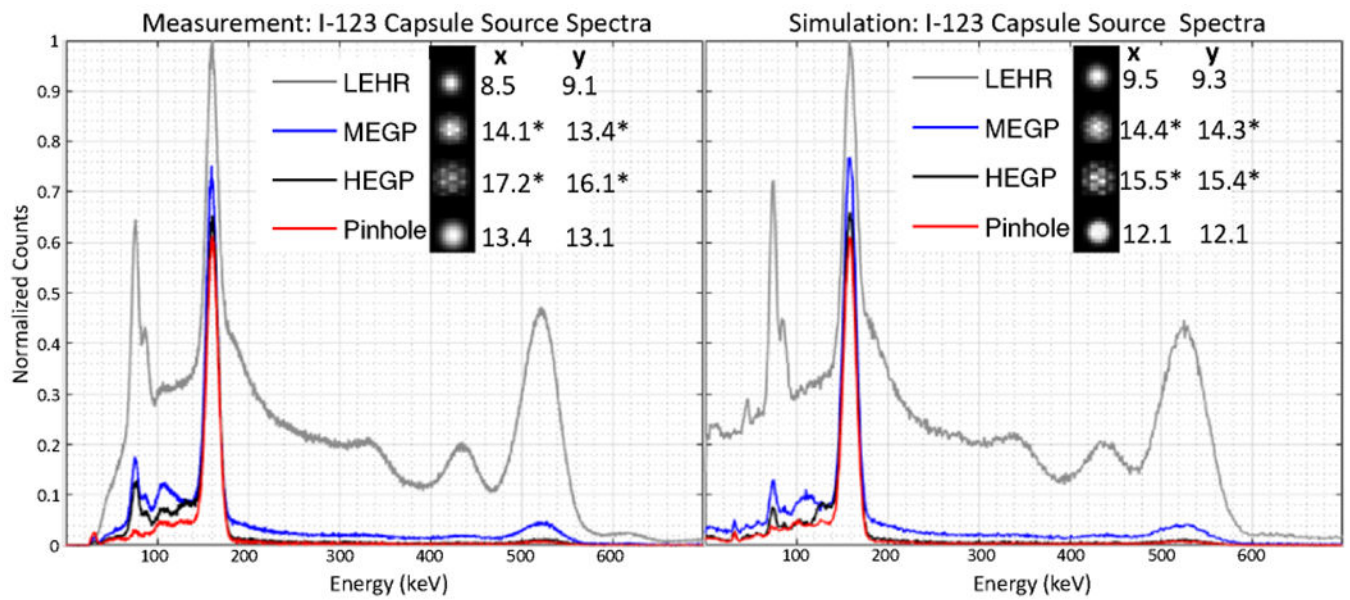
Figure 4.
Measured (left) and simulated (right) energy spectra of an I-123 capsule source at a distance of ~10 cm from the face of the parallel-hole collimators and from the aperture of the pinhole collimator. Both sets of spectra are normalized by the maximum count of the LEHR collimator. The inserts show the corresponding projections and their FWHMs (mm) in horizontal (x) and vertical (y) directions. *The projections of the MEGP and HEGP collimators were smoothed by a Gaussian filter (FWHM: 0.7 mm) prior to FWHM measurement.
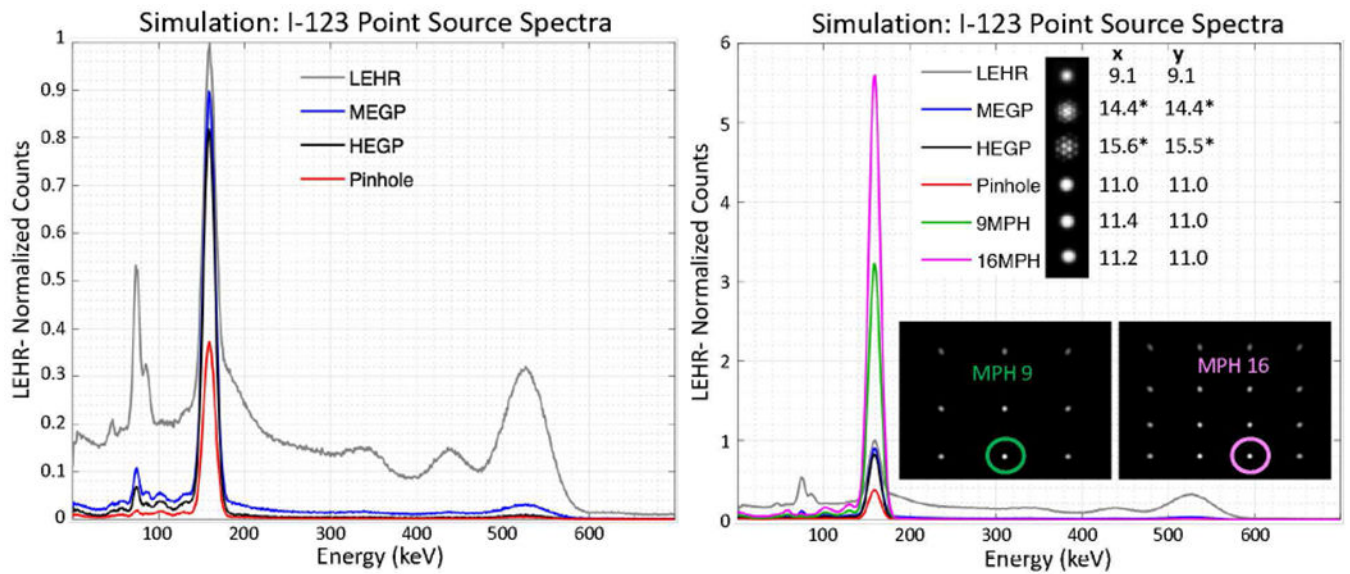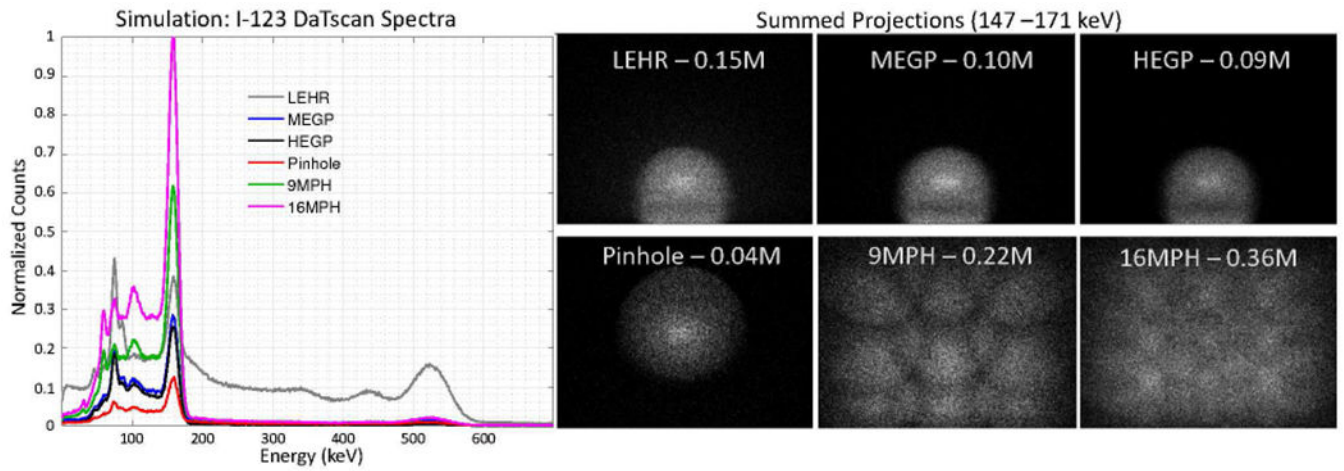
Figure 5.
(Left) Simulated energy spectra of an I-123 point source for the parallel-hole and SPH collimators. (Right) Same data including the spectra from the MPH collimators. Both sets of energy spectra were normalized to the maximum counts of the LEHR collimator. The maximum photopeak counts of the 16MPH is 5.5 times larger than that of LEHR. The inserts show the projections from all collimators and their FWHMs (mm) in horizontal (x) and vertical (y) directions. The FWHMs of the MPH collimators were calculated from the indicated (green and magenta circles) pinhole projections. *The projections of the MEGP and HEGP collimators were smoothed by a Gaussian filter (FWHM: 0.7 mm) prior to FWPIM measurement.

Figure 6.
(Left) Simulated energy spectra of the I-123 DaTscan distribution obtained from parallel-hole and pinhole collimators normalized by the maximum counts of the 16-MPH. (Right) Summed projections over 360° rotation and their total counts obtained within the 15% photopeak window (147 – 171 keV).
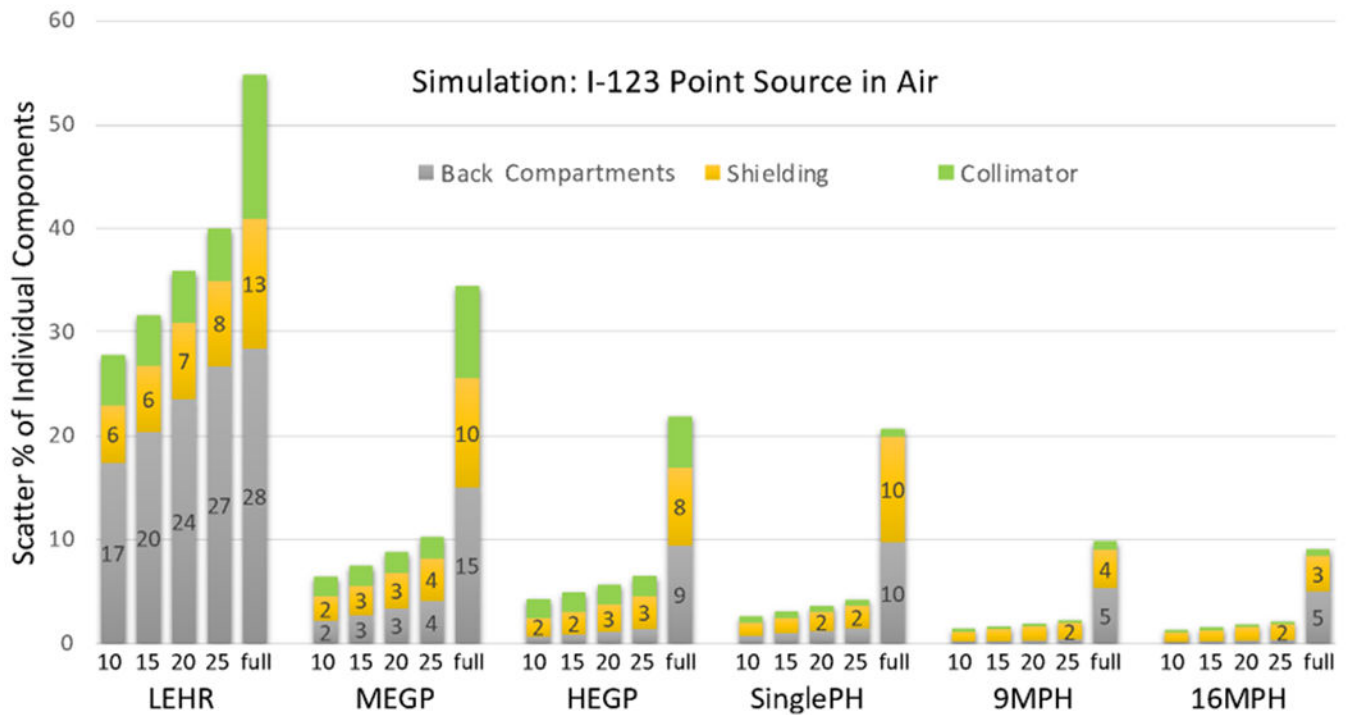
Figure 7.
Scatter fraction in percent *(100 × scatter counts / total counts)* for the I-123 point source from collimator, shielding, and back compartments for different collimators and for a range of photopeak energy windows (10, 15, 20, and 25%) and for the full spectmm (0–700 keV). Only the scatter events from the last volume of interaction were considered. Scatter of below 1.5% is not labeled.
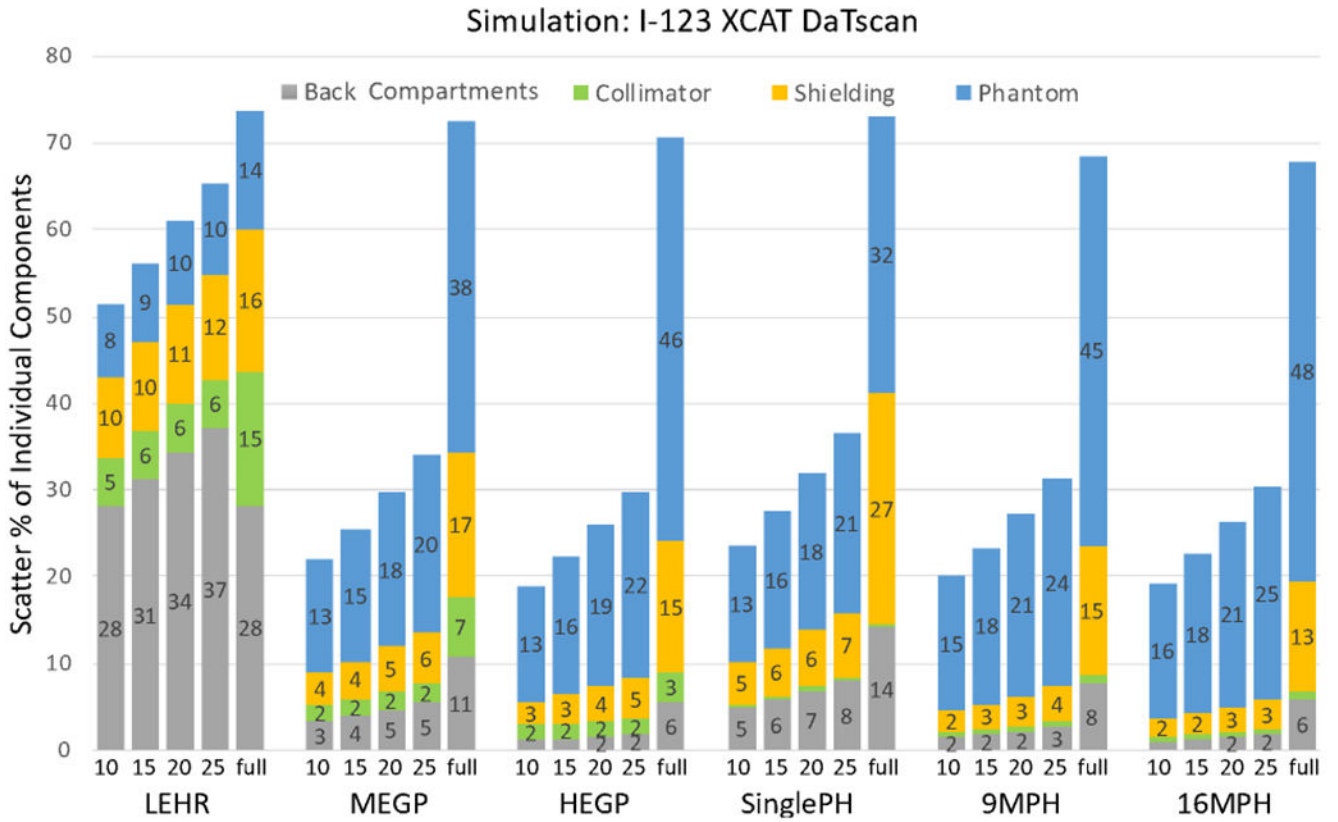
Figure 8.
Scatter fraction in percent *(100 × scatter counts / total counts)* for the I-123 DaTscan simulations from XCAT brain and torso phantom, collimator, shielding, and back compartments for different collimators and for a range of photopeak energy windows (10, 15, 20, and 25%) and for the full spectrum (0–700 keV). Only the scatter events from the last volume of interaction were considered. Scatter of below 1.5% is not labeled.
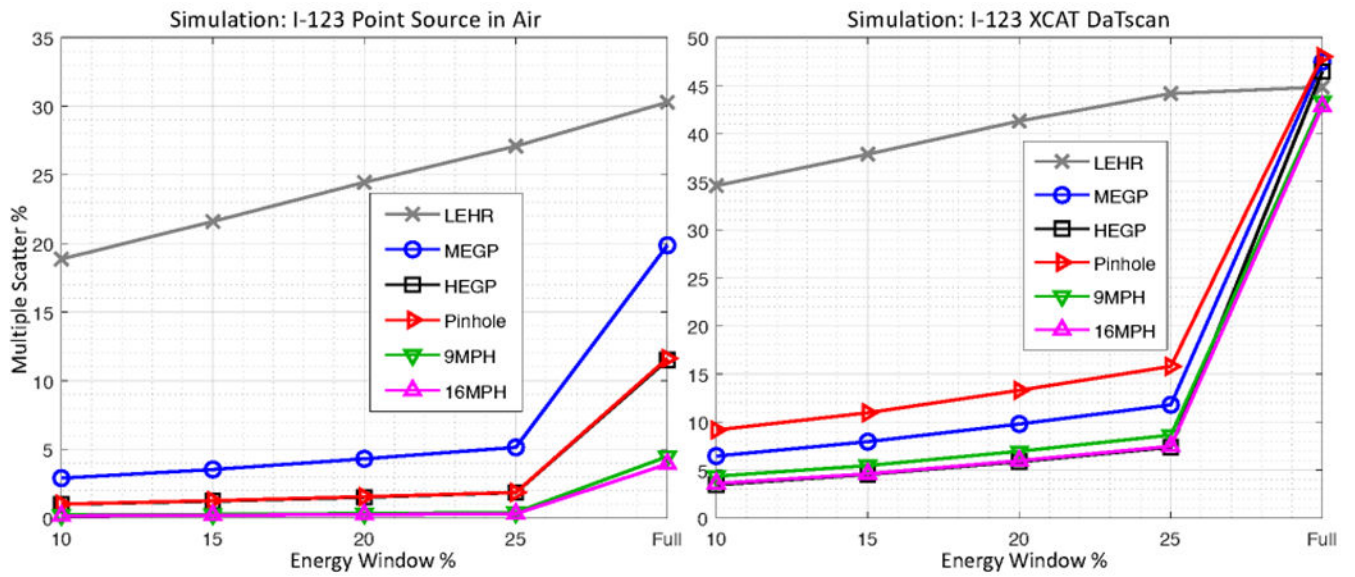
Figure 9.
Multiple scatter fraction in percent *(100× multiple scatter / total counts)* obtained from
the I-123 point source in air (left) and XCAT DaTscan (right) simulations of different
collimators for a range of photopeak energy windows (10, 15, 20, and 25%) and for the full
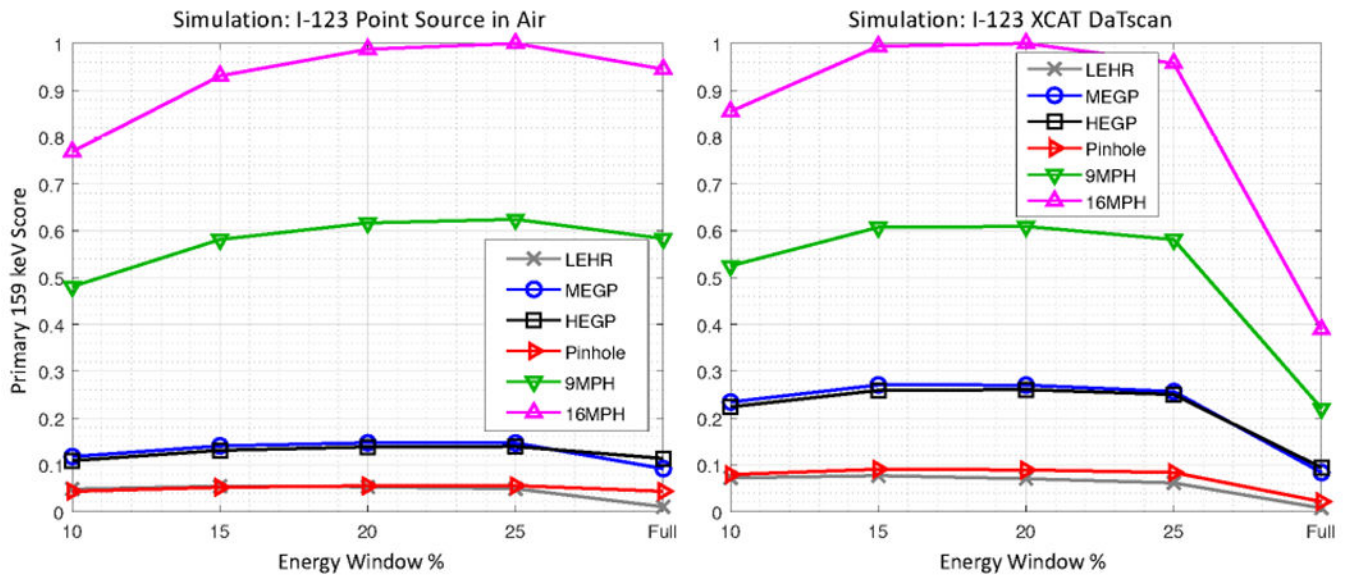spectrum (0–700 keV).

Figure 10.
"Primary 159 keV score" for the I-123 point source (left) and DaTscan (right) simulations, calculated as *(primary$_{159keV}$ / total counts)* × *(primary$_{159keV}$ sensitivity)* and normalized by the maximum value of the 16MPH. Results are shown for a range of photopeak energy windows (10, 15, 20, and 25%) and for the full spectrum (0–700 keV).
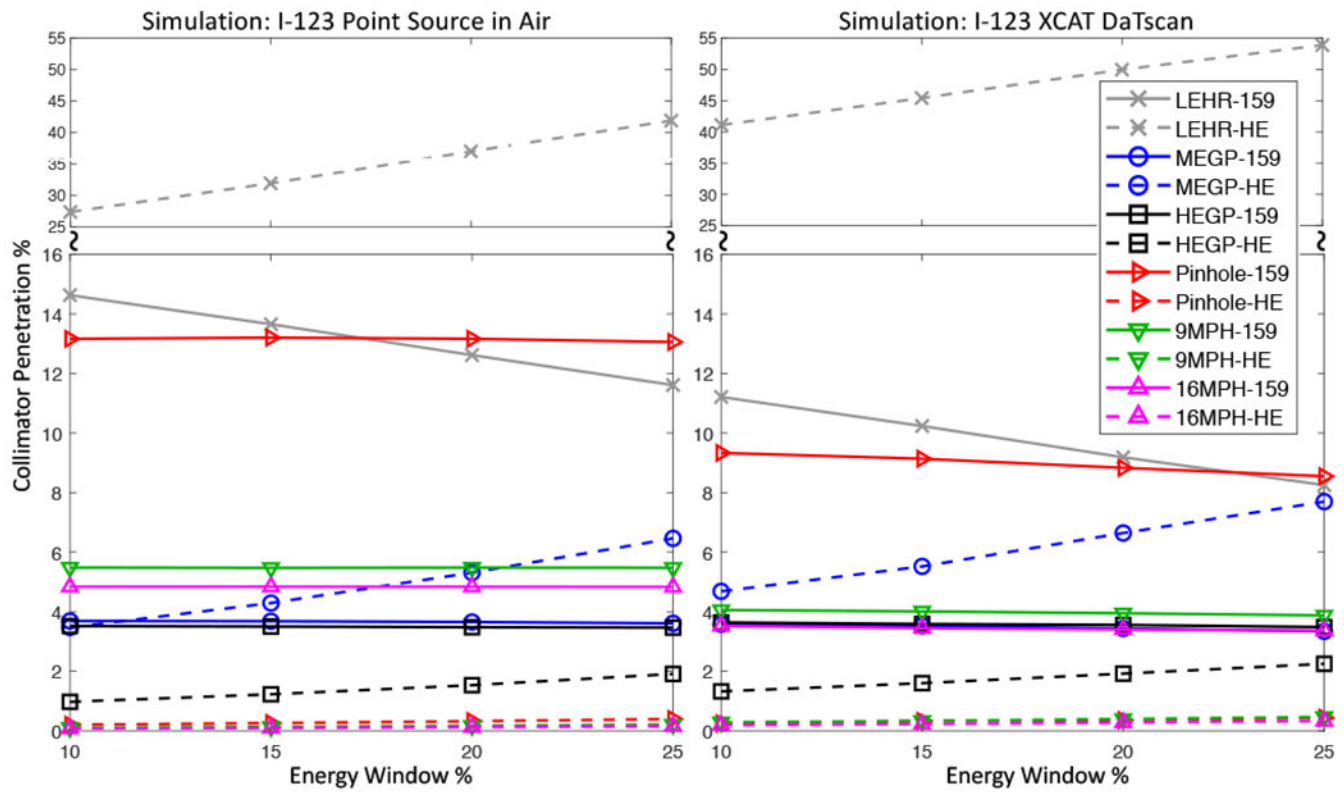
Figure 11.
Collimator penetration in percent *(100 × collimator penetration counts / total counts)* of
the 159 keV and high-energy (HE) photons from the I-123 point source (left) and XCAT
DaTscan (right) simulations for a range of photopeak energy windows (10, 15, 20, and
25%). Note the large amount of penetration through LEHR is observed for the high-energy
emissions (e.g., ~30% for the 15% energy window), while it is negligible for the MPH
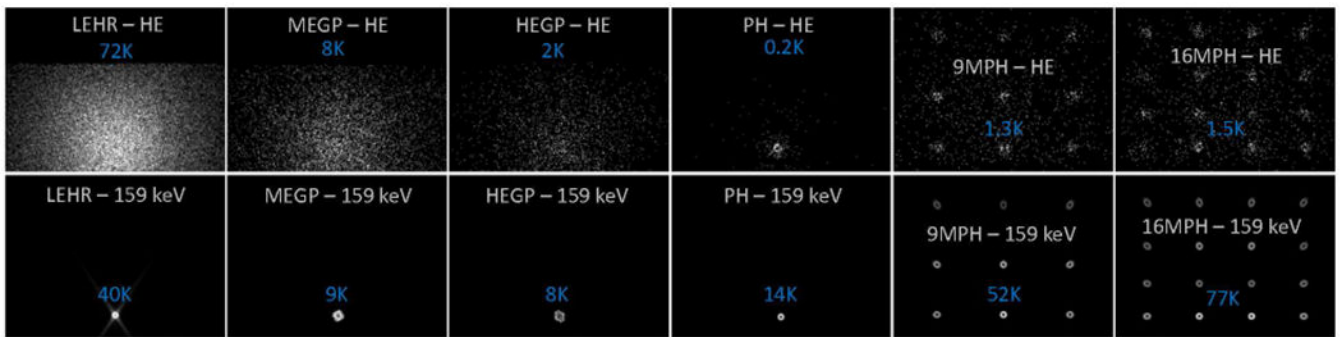collimators.

Figure 12.
Simulated I-123 point source projections of the collimator penetration counts only. The projections in the top row are for the high-energy (HE) photons of I-123 and bottom row are for the 159 keV emissions, obtained within the 15% photopeak energy window. Point source location and imaging time were the same for all cases.

Table 1.

Specifications of the collimators used in experiments and simulations.

	LEHR	MEGP	HEGP	SPH	9MPH, 16MPH
*Hole size (mm)	1.22	3.40	3.81	5.00	5.00
Collimator thickness (cm)	2.70	5.84	5.84	4.15	2
Septal thickness (mm)	0.152	0.86	1.73	–	–
**Air in collimator (%)	74	64	47	10	2.2, 2.5
Collimator material	Lead Alloy	Lead Alloy	Lead Alloy	Lead Alloy	Tungsten Alloy

*
Distance between the two opposite sides of the parallel hexagon holes. Diameter for the SPH and MPH apertures.

**
Derived from the simulated geometry. SPH air% was calculated within the collimator insert.

Table 2.

Summary of the collimator characterizations for the 15% energy window

Simulation: I-123 Point Source in Air				
	LEHR	**MEGP**	**HEGP**	**SPH**	**9MPH, 16MPH**
Total Scatter %	32	8	5	3	1, 1
Multiple Scatter %	22	4	1	1	0, 0
Primary Score %	5	14	13	5	58, 93
Collimator Penetration %	46	8	5	13	6, 5
*Relative Total Count %	1	0.81	0.70	0.33	3.00, 4.75
Simulation: I-123 XCAT DaTscan					
Total Scatter %	56	25	22	28	24, 22
Multiple Scatter %	38	8	5	11	5, 5
Primary Score %	8	27	26	9	61, 99
Collimator Penetration %	56	9	5	9	4, 4
*Relative Total Count	1	0.67	0.60	0.27	1.47, 2.40

*Normalized by total count of LEHR